

DRO: Deep Recurrent Optimizer for Structure-from-Motion

Xiaodong Gu^{1*} Weihao Yuan^{1*} Zuozhuo Dai¹ Siyu Zhu¹ Chengzhou Tang² Ping Tan^{1,2}
¹Alibaba A.I. Labs ²Simon Fraser University

Abstract

There are increasing interests of studying the structure-from-motion (SfM) problem with machine learning techniques. While earlier methods directly learn a mapping from images to depth maps and camera poses, more recent works enforce multi-view geometry through optimization embed in the learning framework. This paper presents a novel optimization method based on recurrent neural networks to further exploit the potential of neural networks in SfM. Our neural optimizer alternatively updates the depth and camera poses through iterations to minimize a feature-metric cost. Two gated recurrent units are designed to trace the historical information during the iterations. Our network works as a zeroth-order optimizer, where the computation and memory expensive cost volume or gradients are avoided. Experiments demonstrate that our recurrent optimizer effectively reduces the feature-metric cost while refining the depth and poses. Our method outperforms previous methods and is more efficient in computation and memory consumption than cost-volume-based methods. The code of our method will be made public.

1. Introduction

Structure-from-motion (SfM) [30] is a fundamental task in computer vision and essential for numerous applications such as robotics, autonomous driving, augmented reality, and 3D reconstruction. Given a sequence of images, SfM methods optimize depth maps and camera poses to recover the 3D structure of a scene. Traditional methods solve the Bundle-Adjustment (BA) problem [35], where the reprojection error between reprojected 3D scene points and 2D image feature points are minimized iteratively.

Recently, deep-learning-based methods have dominated most benchmarks and demonstrated advantages over traditional methods [36, 17, 32, 21, 40, 33]. Earlier learning-based methods [36, 14, 23, 26] directly regress the depth maps and camera poses from the input images, but the domain knowledge such as multi-view geometry is ignored. To combine the strength of neural networks and traditional geometric methods, more recent works formulate the

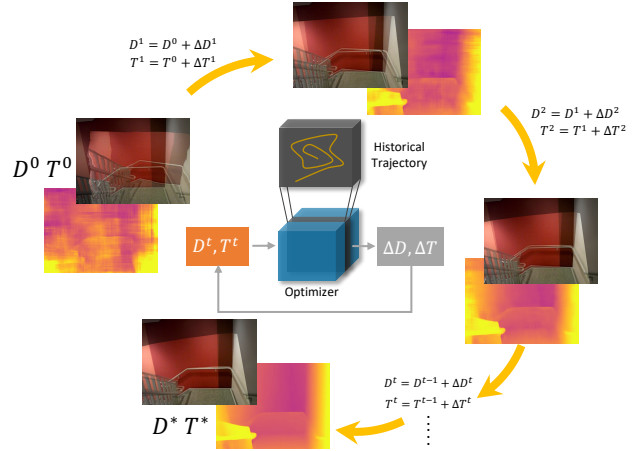


Figure 1: A gated recurrent network (indicated as the optimizer in the middle) iteratively updates a depth map and the relative motion between two images by minimizing a feature-metric cost. At each iteration, we show a color-coded depth map and a superimposed image generated from the two input images according to the depth map and camera motion. Over the iterations, the superimposed image becomes gradually sharper while the depth map improves.

geometric-based optimization as differentiable layers and embed them in a learning framework [32, 33, 45].

We follow the approach of combining neural networks and optimization methods with some novel insights. Firstly, previous methods [32, 12, 33] adopt gradient-based optimization such as Levenberg-Marquardt or Gauss-Newton methods. However, the gradients could be noisy and misleading especially for the high-dimensional optimization problem in dense depth map computation. Careful regularization such as the depth bases [32] or manifold embedding [6, 7] is often required. Furthermore, a multi-resolution strategy is needed to gradually compute the solution from coarse to fine. In comparison, we employ a gated recurrent neural network for optimization as inspired by [34] as illustrated in Figure 1. Our method does not compute gradients and works on the high resolution image directly without regularization which might limit the algorithm generalization.

Secondly, some methods [40, 33, 48, 45] build cost volumes to solve the dense depth maps. Similar cost volume is also employed in [34] to compute optical flow. A cost vol-

*Equal contribution.

ume encodes the errors of multiple different depth values at each pixel. It evaluates the result quality within a large spatial neighborhood in the solution space in a discrete fashion. While cost volumes have been demonstrated effective in computing depth maps [43, 20, 40], they are inefficient in time and space because they exhaustively evaluate results in a large spatial neighborhood. We argue that a gated recurrent network [11] can minimize the feature-metric error to compute dense depth without resorting to compute such a cost volume. In particular, the gated recurrent network only looks at the result quality at the current solution (i.e. a single point in the solution space) and those of the previous iterations to update the results. In spirit, our learned optimizer is zeroth-order and exploits temporal information during iterations, while gradient based methods or cost volume based methods rely only on the spatial information. In this way, our method has the potential of better running time and memory efficiency.

In experiments, our method demonstrates better accuracy than previous methods in both indoor and outdoor data. Our method is good at dealing with small-size, thin, and distinct objects. We also show that the recurrent optimizer reduces the feature-metric cost over iterations and produces gradually improved depth maps and camera poses.

Our contributions can be summarized as follows:

- 1) We propose a novel zeroth-order recurrent optimizer for joint depth and camera pose optimization where gradients or cost volumes are not involved for better memory and computation efficiency.
- 2) The depths and poses are alternatively updated to uncouple the mutual influence by the GRU module for effective optimization.
- 3) Our optimizer outputs better results than previous methods in both supervised and self-supervised settings.

2. Related work

Supervised Deep SfM. Deep neural networks can learn to solve the SfM problem directly from data [36, 48, 40]. With the ground-truth information, DeMoN [36] trains two network branches to regress structures and motions separately with an auxiliary flow prediction task to exploit feature correspondences. Some methods adopt a discrete sampling strategy to achieve high-quality depth maps [48, 33]. They generate depth hypotheses and utilize multiple images to construct a cost volume. Furthermore, the pose volume is also introduced in [40]. They take the feature maps to build two cost volumes and employ 3D convolutions to regularize.

There are also methods to directly regress scene depth from a single input image [14, 17, 26], which is an ill-posed problem. These methods rely heavily on the data fitting of the neural networks. Therefore, their network structure and feature volumes are usually bulky, and their performance

are limited in unseen scenes.

Self-supervised Deep SfM. Supervised methods, nevertheless, require collecting a large number of training data with ground-truth depth and camera poses. Recently, many unsupervised works [49, 18, 28, 46, 27, 37, 42, 44, 29, 4, 21, 38] have been proposed to train a depth and pose estimation model from only monocular RGB images. They employ the predicted depths and poses to warp the neighbor frames to the reference frame, such that a photometric constraint is created to serve as a self-supervision signal. In this case, the dynamic objects is a problem and would generate errors in the photometric loss. To address this, semantic mask [24] and optical flow [50, 47, 5] are proposed to exclude the influence of moving objects. Another challenge is the visibility problem between different frames. To deal with this, a minimum re-projection loss are designed in [18, 21] to handle the occluded regions. Despite these efforts, there is still a gap between the self-supervised methods and the supervised methods.

Learning to Optimize. Traditional computer vision methods usually formulate the tasks as optimization problems according to the first principles such as photo-consistency, multi-view geometry, etc. Inspired by this, recently many works are seeking to combine the strength of neural network and traditional optimization-based methods. There are mainly two approaches in learning to optimize. One approach [3, 2, 32, 33] employs a network to predict the inputs or parameters of an optimizer, which is implemented as some layers in a large neural network for end-to-end training. On the contrary, the other approach directly learns to update optimization variables from the data [1, 9, 16, 12, 34].

However, the first approach needs to explicitly formulate the solver and is limited to problems where the objective function can be easily defined [3, 2, 32, 33]. Furthermore, the methods in [12, 32] need to explicitly evaluate gradients of the objective function, which is hard in many problems. Besides, the methods in [33, 34] adopt cost volumes, which make the model heavy to apply.

In comparison, our method does not require gradients computation or cost volume aggregation. It only evaluates the result quality at a single point in the solution space at each step. In this sense, it is a zeroth-order optimizer embedded in a network. By accumulating temporal evidence from previous iterations, our GRU module learns to minimize the objective function. Unlike the method in [34] which still relies on a cost volume, our method is more computation and memory efficient. Besides, two updaters in our framework, one for depth and the other one for pose, are alternatively updated, which is inspired by the traditional bundle adjustment algorithm.

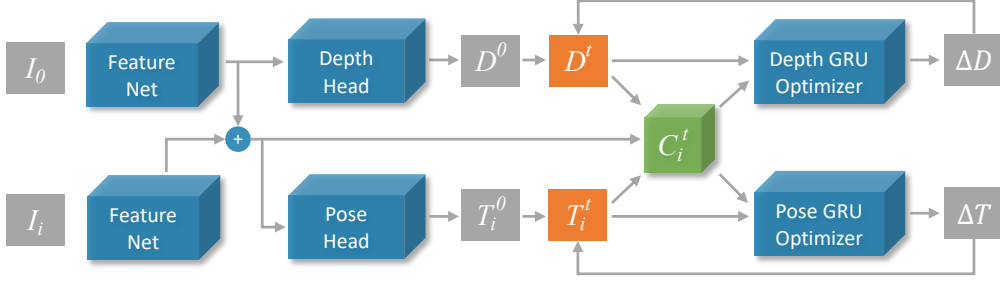


Figure 2: The overview of our framework. The reference image I_0 and context image I_i are first fed into feature networks sharing the same parameters, then the extracted features are mapped to the initial depth prediction D^0 and the initial pose prediction T_i^0 by the depth head and the pose head, respectively. Afterwards the optimizer begins to update the depth and pose iteratively. The current depth D^t , current pose T_i^t , and features of images are utilized to build the cost C_i^t , then they are all fed into the optimizer to output the variables increments. By iteratively adding the increments, the estimated depth and pose would progressively converge to the optimum, D^* and T^* .

3. Deep Recurrent Optimizer

3.1. Overview

Given the reference image I_0 and N neighboring images $\{I_i\}_{i=1}^N$, our method outputs the depth D of the reference image and the relative camera poses $\{T_i\}_{i=1}^N$ for images $\{I_i\}_{i=1}^N$ as shown in Figure 2. Images are first fed into a shared feature extraction module to produce features \mathcal{F}_i for each image, then a depth head and a pose head take these features in and output the initial depth map and relative poses. Finally, the initial depth map and relative poses are refined by the depth and the pose GRU-optimizers alternatively, and converge to the final depth and poses.

3.2. Feature Extraction and Cost Construction

Similar to BA-Net [32], we construct a photometric cost in feature space as the energy function to minimize. This cost measures the distance between aligned feature maps. Given the depth map D for the reference image I_0 and the relative camera pose T_i of I_i respect to I_0 , the cost is defined at each pixel x in the reference image I_0 :

$$C_i(x) = \|\mathcal{F}_i(\pi(T_i, D(x) \cdot \pi^{-1}(x))) - \mathcal{F}_0(x)\|_2, \quad (1)$$

where $\|\cdot\|_2$ is the L2 norm, and π is the projection function. Thus, $D(x) \cdot \pi^{-1}(x)$ is the 3D point corresponding to the pixel location x , and T_i transforms 3D points from the camera space of the image I_0 to that of I_i . Note that the feature-metric error in BA-Net [32] would further sum the cost over all pixels as $\sum_x C_i(x)$. However, in this work, we maintain a cost map $C(x)$ that has the same resolution with the feature map \mathcal{F}_i . In the following of this paper, we refer $C(x)$ as cost map instead of feature-metric error.

Depth and pose cost. When there are multiple neighboring images, we average multiple cost values $\{C_i(x)\}_{i=1}^N$ as $C_d(x)$ for the depth value at each pixel:

$$C_d(x) = \frac{1}{N} \sum_{i=1}^N C_i(x). \quad (2)$$

For the pose cost, we directly use $C_i(x)$ on each image I_i because the pose T_i only associates with I_i when the depth map D is fixed in our alternative optimization.

Feature extraction. There are two feature extraction modules. One is denoted as base feature network for extracting the aforementioned feature maps $\{\mathcal{F}_i\}_{i=0}^N$, while the other one is denoted as contextual feature network for providing the initial hidden state and the contextual feature for the GRU optimizer. We use ResNet18 [22] as our backbone to extract features. The resolution of the feature maps is 1/8 of the original input images. The feature of the reference image is used for depth branch, while the feature of the concatenated image pair is used for pose branch.

3.3. Iterative Optimization

We then minimize the cost map C_d in an iterative manner. At each iteration, the optimizer outputs an update of the depth ΔD and that of the pose ΔT . Inspired by [34], we utilize a gated recurrent unit to compute these updates, since a GRU can memorize the status at the previous results during the optimization and the gated activation makes the update easier to converge.

3.3.1 Initialization

The initial depth and pose are from two simple initial networks, which are adding a depth head and a pose head upon the base feature network, respectively. The depth head is composed of two convolutional neural layers, and the pose head is plus another average pooling layer. The hidden state is initialized by the contextual feature network, with the tanh function as the activation.

3.3.2 Recurrent Update

We design two GRU modules, one for updating the depth and the other one for updating the camera pose. Each GRU module receives the current cost map C^{t-1} and the current

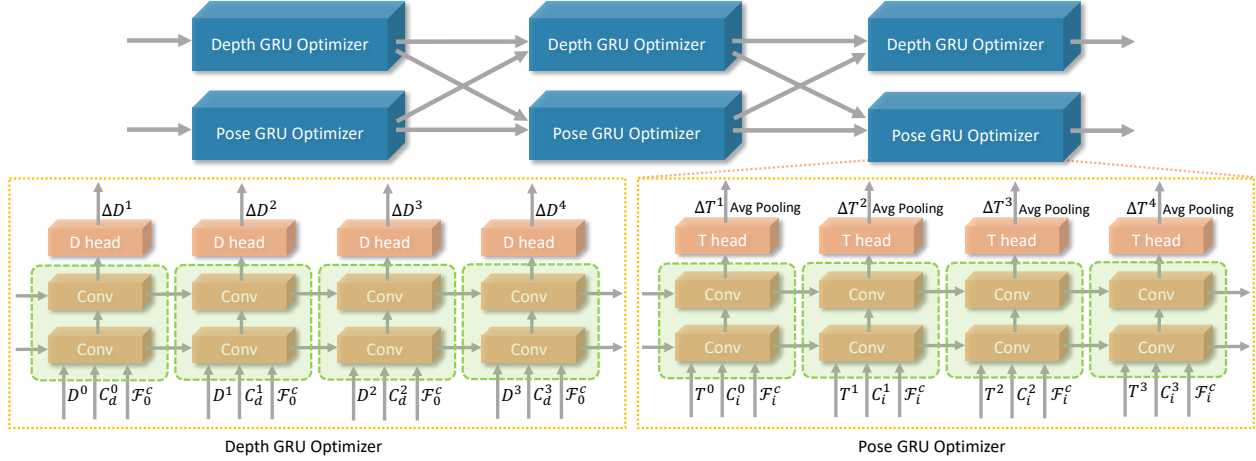


Figure 3: Working flow of the optimizer. Updating of the depth and the pose are separated in each stage, where 4 updates of the depth are followed by 4 updates of the pose. We adopt 3 stages in our framework. For each update for the depth, the predicted depth \mathbf{D}^{t-1} , cost \mathbf{C}_d^{t-1} , and contextual feature map \mathcal{F}_0^c are fed in, then the update $\Delta \mathbf{D}^t$ is predicted based on the inputs and historical information. Afterwards, the depth is updated by $\mathbf{D}^t = \mathbf{D}^{t-1} + \Delta \mathbf{D}^t$.

estimated variables \mathbf{V}^{t-1} (depth map \mathbf{D}^{t-1} or camera pose \mathbf{T}^{t-1}) and outputs an incremental update $\Delta \mathbf{V}^t$ to update the results as $\mathbf{V}^t = \mathbf{V}^{t-1} + \Delta \mathbf{V}^t$.

Specifically, we first project the variable \mathbf{V}^{t-1} and the cost \mathbf{C}^{t-1} into the feature space with two convolutional layers \mathcal{P}_v and \mathcal{P}_c respectively, and then concatenate $\mathcal{P}_v(\mathbf{V}^{t-1})$, $\mathcal{P}_c(\mathbf{C}^{t-1})$, and the image contextual feature \mathcal{F}^c into \mathbf{M}^{t-1} . Therefore, the structure inside each GRU unit is as follows:

$$\begin{aligned} z^t &= \sigma(\text{Conv}_{5 \times 5}([h^{t-1}, \mathbf{M}^{t-1}], W_z)) \\ r^t &= \sigma(\text{Conv}_{5 \times 5}([h^{t-1}, \mathbf{M}^{t-1}], W_r)) \\ \tilde{h}^t &= \tanh(\text{Conv}_{5 \times 5}([r^t \odot h^{t-1}, x^{t-1}], W_h)) \\ h^t &= (1 - z^t) \odot h^{t-1} + z^t \odot \tilde{h}^t, \end{aligned} \quad (3)$$

where $\text{Conv}_{5 \times 5}$ represents a separable 5×5 convolution, \odot is the element-wise multiplication, σ and \tanh are the sigmoid and the tanh activation functions. Finally, the depth maps or the camera poses are predicted from the hidden state h^t by similar structures to the initial depth or the camera pose head in Sec. 3.3.1.

With this optimizer, from the initial point, the estimated depth and pose are iteratively refined as the optimization iteration proceeds. Finally they will both converge to fixed points $\mathbf{D}^t \rightarrow \mathbf{D}^*$ and $\mathbf{T}^t \rightarrow \mathbf{T}^*$.

3.3.3 Alternative Optimization

After defining the structure of the GRU unit, we update the depth map \mathbf{D}^t and the camera transformation \mathbf{T}^t alternatively in totally m stages. As shown in Figure 3, at each stage, we first freeze the camera pose and update the depth map as $\mathbf{D}^t = \mathbf{D}^{t-1} + \Delta \mathbf{D}^t$, which is repeated by n times.

Then we freeze the depth map \mathbf{D} and switch to the camera pose updating, where $\mathbf{T}^t = \mathbf{T}^{t-1} + \Delta \mathbf{T}^t$ is also repeated by n times. This alternative optimization leads to more stable optimization and easier training empirically. In our experiments, m is set as 3 and n is set as 4 if not particularly specified.

To gain more insights into the recurrent process and demonstrate the GRU unit behaves as a recurrent optimizer, we visualize how the feature-metric error decreases over the GRU iterations in Figure 4. This figure shows that both the depths and the poses are refined step-by-step to the optimum along with a decreasing cost. Eventually, the warped neighbor image is aligned seamlessly with the reference image, and the estimated depth is close to the ground truth. This indicates that our optimizer refines the outputs by learning to minimize the feature-metric error.

3.4. Training Loss

3.4.1 Supervised Case

When ground truth is available, we supervise the training by evaluating the depth and pose errors.

Depth supervision $\mathcal{L}_{\text{depth}}$ computes the L1 distance between the predicted depth map \mathbf{D} and the ground-truth depth map $\hat{\mathbf{D}}$ in each stage:

$$\mathcal{L}_{\text{depth}} = \sum_{s=1}^m \gamma^{m-s} \|\mathbf{D}^s - \hat{\mathbf{D}}\|_1, \quad (4)$$

where γ is a discounting factor.

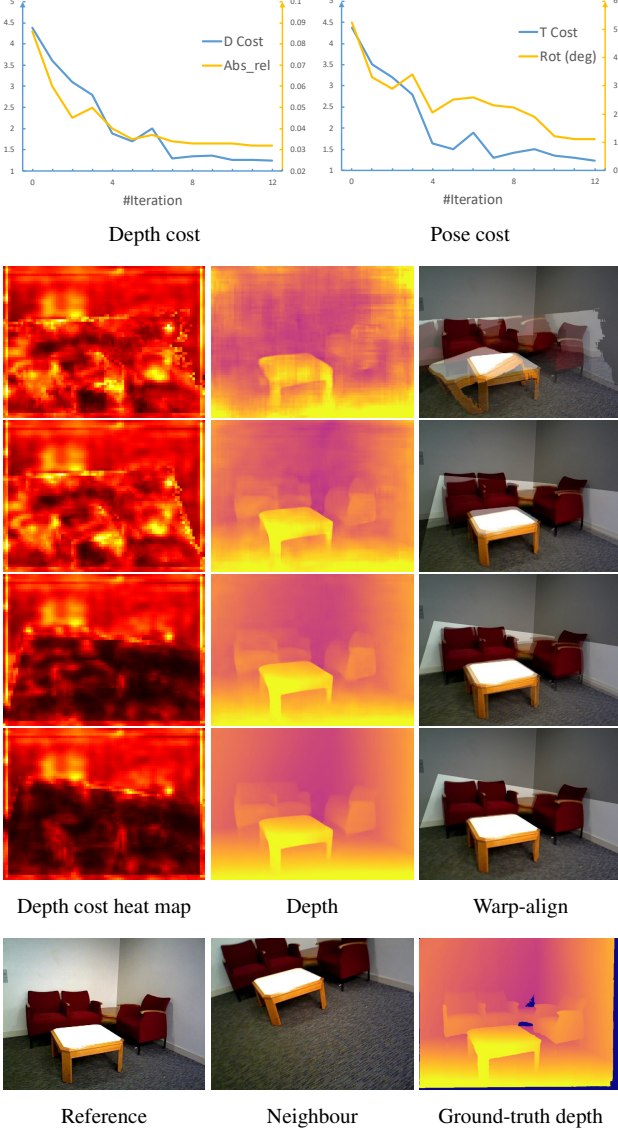


Figure 4: Visualization of the cost decreasing with regards to the stage of the GRU optimizer. From the cost heat map, the cost of the aligned region, e.g., the desk, keeps falling. In the meantime, we display how the depth and the pose are refined gradually. The aligned image warping the neighbor image onto the reference image using the estimated depth and pose is also presented.

Pose supervision $\mathcal{L}_{\text{pose}}$ is defined as the following according to the ground truth depth \hat{D} and pose \hat{T}_i :

$$\sum_{s=1}^m \sum_x \gamma^{m-s} \|\pi(\mathbf{T}_i^s, \hat{D}(x) \cdot \pi^{-1}(x)) - \pi(\hat{T}_i, \hat{D}(x) \cdot \pi^{-1}(x))\|_1. \quad (5)$$

This loss computes the image projection of a pixel x according to the estimated pose \mathbf{T}^s and the true pose \hat{T} in each stage. The distance between these two projections is

defined as the pose loss, which is in the image coordinate and insensitive to different scene scales. In the experiments we find it is more effective than directly comparing the difference between \mathbf{T}^s and \hat{T} in the experiments.

Then the supervised loss is the sum of these two terms:

$$\mathcal{L}_{\text{supervised}} = \mathcal{L}_{\text{depth}} + \mathcal{L}_{\text{pose}}. \quad (6)$$

3.4.2 Self-supervised Case

When ground truth is not available, we borrow the loss defined in [19] for self-supervised training. Specifically, the supervision signal comes from geometric constraints and is composed of two terms, a photometric loss and a smoothness loss.

Photometric loss $\mathcal{L}_{\text{photo}}$ measures the similarity of the reconstructed images $\{\mathbf{I}'_i\}_{i=1}^N$ to the reference image \mathbf{I}_0 . Here, the reconstructed images \mathbf{I}'_i are generated by warping the input image \mathbf{I}_i according to the depth D and pose \mathbf{T}_i . This similarity is measured by the structural similarity (SSIM) [39] with L1 loss as

$$\mathcal{L}_{\text{photo}} = \alpha \frac{1 - SSIM(\mathbf{I}'_i, \mathbf{I}_0)}{2} + (1 - \alpha) \|\mathbf{I}'_i - \mathbf{I}_0\|_1, \quad (7)$$

where α is a weighting factor. For the fusion of multiple photometric losses, we also take the strategies defined in [19], which adopts a minimum fusion and masks stationary pixels.

Smoothness loss $\mathcal{L}_{\text{smooth}}$ encourages adjacent pixels to have similar depths, especially for those with a similar color:

$$\mathcal{L}_{\text{smooth}} = |\partial_x D| e^{-|\partial_x I_0|} + |\partial_y D| e^{-|\partial_y I_0|}. \quad (8)$$

Then the self-supervision loss is defined by a weighted sum of these two terms:

$$\mathcal{L}_{\text{self}} = \mathcal{L}_{\text{photo}} + \lambda \mathcal{L}_{\text{smooth}}. \quad (9)$$

where λ enforces a weighted depth regularization.

4. Experiments

This section first presents the implementation details and then evaluates our supervised and self-supervised models on outdoor and indoor datasets, which are followed by the ablation studies.

4.1. Implementation Details

Our work is implemented in Pytorch and trained on Nvidia GTX 2080 Ti GPUs. The network is optimized end-to-end with Adam ($\beta_1 = 0.9$, $\beta_2 = 0.999$) and the learning rate decreases from 2×10^{-4} to 5×10^{-5} in 50 epochs.

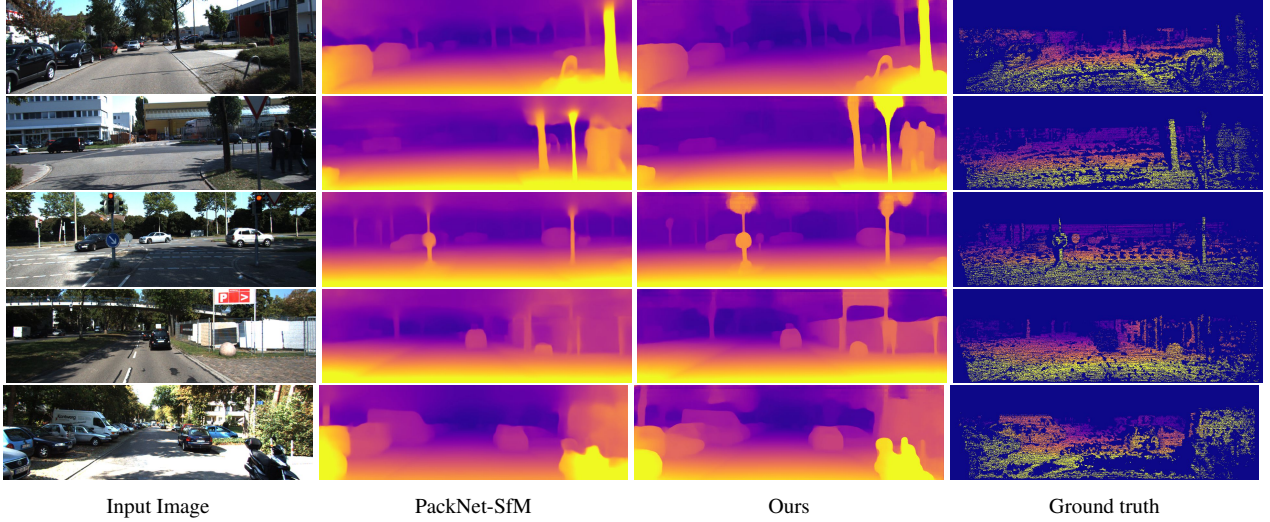


Figure 5: Qualitative results on the KITTI dataset.

Method	Input	Supervised	GT type	Abs Rel	Sq Rel	RMSE	RMSE _{log}	$\delta < 1.25$	$\delta < 1.25^2$	$\delta < 1.25^3$
MonoDepth [18]	M→O	✗	Improved	0.090	0.545	3.942	0.137	0.914	0.983	0.995
PackNet-SfM [21]	M→O	✗	Improved	0.071	0.359	3.153	0.109	0.944	0.990	0.997
DRO (ours)	Multi	✗	Improved	0.057	0.342	3.201	0.123	0.952	0.989	0.996
Kuznetsov et al. [25]	One	✓	Improved	0.089	0.478	3.610	0.138	0.906	0.980	0.995
DORN [17]	One	✓	Improved	0.072	0.307	2.727	0.120	0.932	0.984	0.995
PackNet-SfM [21]	M→O	✓	Improved	0.064	0.300	3.089	0.108	0.943	0.989	0.997
BANet [32]	Multi	✓	Improved	0.083	—	3.640	0.134	—	—	—
DeepV2D (2-view) [33]	Multi	✓	Improved	0.064	0.350	2.946	0.120	0.946	0.982	0.991
DRO (ours)	Multi	✓	Improved	0.047	0.199	2.629	0.082	0.970	0.994	0.998
SfMLearner [49]	M→O	✗	Velodyne	0.208	1.768	6.856	0.283	0.678	0.885	0.957
CCNet [29]	M→O	✗	Velodyne	0.140	1.070	5.326	0.217	0.826	0.941	0.975
GLNet [10]	M→O	✗	Velodyne	0.135	1.070	5.230	0.210	0.841	0.948	0.980
MonoDepth [18]	M→O	✗	Velodyne	0.115	0.882	4.701	0.190	0.879	0.961	0.982
PackNet-SfM [21]	M→O	✗	Velodyne	0.107	0.803	4.566	0.197	0.876	0.957	0.979
DRO (ours)	Multi	✗	Velodyne	0.088	0.797	4.464	0.212	0.899	0.959	0.980
PackNet-SfM [21]	M→O	✓	Velodyne	0.090	0.618	4.220	0.179	0.893	0.962	0.983
DRO (ours)	Multi	✓	Velodyne	0.073	0.528	3.888	0.163	0.924	0.969	0.984

Table 1: Quantitative results on the KITTI dataset. Eigen split is used for evaluation and seven widely used metrics are reported. Results on two ground-truth types are displayed since different methods are evaluated using different types. ‘M→O’ means multiple images are used in the training while one image is used for inference.

For supervised training, we use the ground truth from the datasets to supervise the training with the losses described in section 3.4.1, where γ is set as 0.85. For self-supervised training, without any ground-truth information, geometric constraints are leveraged to provide the supervision as depicted in section 3.4.2, where α is set as 0.85 and λ is set as 0.01.

4.2. Datasets

KITTI dataset. The KITTI dataset is a widely used benchmark for depth evaluation, where outdoor scenes are captured from a moving vehicle. We adopt the training/test

split proposed by Eigen et al. [14], resulting in 22,600 images for training and 697 images for testing. There are two types of ground-truth depth. One is the original Velodyne Lidar points which are quite sparse. The other one is the improved annotated depth map, which uses five successive images to accumulate the Lidar points and stereo images to handle moving objects. For the improved depth type there are 652 images for testing.

ScanNet dataset. ScanNet [13] is a large indoor dataset consisting of 1,513 RGB-D videos in 707 distinct environments. The raw data is captured from a depth camera. The

Method	Supervised	Abs Rel	Sq Rel	RMSE	RMSE _{log}	SI Inv	Rot (deg)	Tr (deg)	Tr (cm)	Time (s)
Photometric BA [15]	✓	0.268	0.427	0.788	0.330	0.323	4.409	34.36	21.40	—
DeMoN [36]	✓	0.231	0.520	0.761	0.289	0.284	3.791	31.626	15.50	—
BANet [32]	✓	0.161	0.092	0.346	0.214	0.184	1.018	20.577	3.39	—
DeepV2D (2-view) [33]	✓	0.069	0.018	0.196	0.099	0.097	0.692	11.731	1.902	0.95
DRO (ours)	✗	0.140	0.127	0.496	0.212	0.210	0.691	11.702	1.647	0.11
DRO (ours)	✓	0.053	0.017	0.168	0.081	0.079	0.473	9.219	1.160	0.11

Table 2: Quantitative results on the ScanNet dataset. Five metrics of the depth and three metrics of the pose are reported.

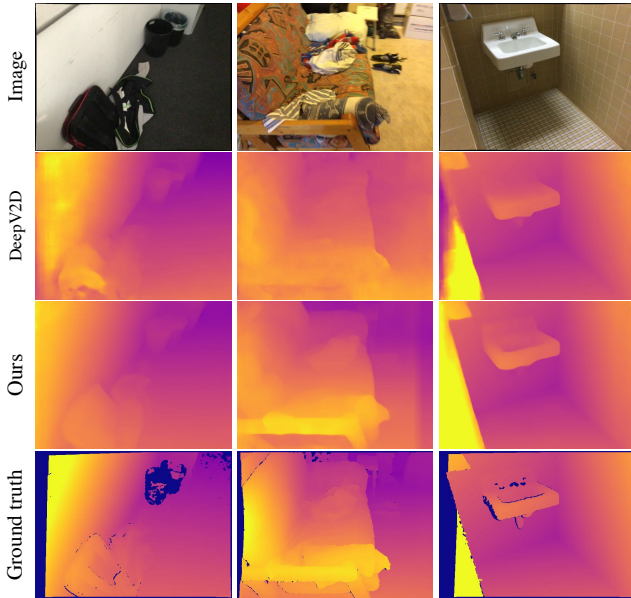


Figure 6: Qualitative results on the ScanNet dataset.

depth maps and camera poses are obtained from RGB-D 3D reconstruction. We use the training/testing split proposed by [32], where 2,000 image sequences from 90 scenes are used for test. In each test sequence, there are 2 images for inference.

SUN3D, RGB-D SLAM, and Scenes11. SUN3D [41] has some indoor scenes where the imperfect depths and poses are provided. RGB-D SLAM [31] provides high-quality camera poses obtained with an external motion-tracking system and noisy depth maps. Scenes11 [36] is a synthetic dataset generated from ShapeNet [8] with perfect depths and camera poses. For these datasets, we use the data processed and split by [36] for a fair comparison to previous methods, resulting in 29,183 image sequences for training and 80 image sequences for testing in SUN3D, 3,351 image sequences for training and 80 image sequences for testing in RGB-D SLAM, 17,353 image sequences for training and 128 image sequences for testing in Scenes11.

4.3. Evaluation

Evaluation on KITTI. For outdoor scenes, we present the results of our method and some previous methods on

the KITTI dataset in Table 1. State-of-the-art single-frame depth estimation methods and deep SfM methods are listed. For a fair comparison, all SfM methods are evaluated under the two-view setting. From the results, our approach outperforms other methods by a large margin in both the supervised setting and the self-supervised setting. Also, the performance of our self-supervised model already surpasses most previous supervised methods. The qualitative results of these outdoor scenes are shown in Figure 5, from which we can see our approach estimates better depth for distant and small-size or thin objects, e.g., people, motorbike, and guidepost. Also, we predict sharper edges at object boundaries. Thin structures are usually recovered by fine updates in the last few iterations.

Evaluation on ScanNet. For indoor scenes, we evaluate our method on the ScanNet dataset in Table 2. For a fair comparison, all methods are evaluated under the two-view setting since there are only 2 images in the testing split. The results of Photometric BA and DeMoN are cited from [32]. The results show that our model outperforms previous methods on both depth accuracy and pose accuracy. Our self-supervised model is already able to predict the results that are comparable to supervised methods, especially on the pose accuracy. Among previous methods, DeepV2D performs best but it requires pre-training a complex pose solver first. Also, the inference time of their method is much longer than ours. Even using five views their performance is still not comparable to ours, of which their depth error is 0.057. From the qualitative results shown in Figure 6, our model predicts the finer depth of the indoor objects and is robust in clutter.

Evaluation on SUN3D, RGB-D SLAM, and Scenes11. We further evaluate our approach on the SUN3D, RGB-D SLAM, and Scenes11 datasets using the data pre-processed by [36] for a fair comparison. In the experiments, however, we find some of the picked image sequences are not suitable for training an SfM model because there is not enough overlap between neighbor images, which especially influences the prediction of the depth maps. Still, we achieve decent performance that is comparable to previous methods, especially in the pose accuracy, which is not seriously affected by the lack of overlap.

Method	SUN3D					RGB-D					Scenes11				
	L1-inv	Sc-inv	L1-rel	Rot	Tran	L1-inv	Sc-inv	L1-rel	Rot	Tran	L1-inv	Sc-inv	L1-rel	Rot	Tran
DeMoN [36]	0.019	0.114	0.172	1.801	18.811	0.028	0.130	0.212	2.641	20.585	0.019	0.315	0.248	0.809	8.918
LS-Net [12]	0.015	0.189	0.650	1.521	14.347	0.019	0.090	0.301	1.010	22.100	0.010	0.410	0.210	0.910	8.210
BANet [32]	0.015	0.110	0.060	1.729	13.260	0.008	0.087	0.050	2.459	14.90	0.080	0.210	0.130	1.298	10.370
DeepSfM [40]	0.013	0.093	0.072	1.704	13.107	0.011	0.071	0.126	1.862	14.570	0.007	0.112	0.064	0.403	5.828
DRO (ours)	0.011	0.108	0.076	1.334	10.988	0.004	0.087	0.046	2.839	11.390	0.010	0.167	0.096	0.366	3.705

Table 3: Quantitative results on the SUN3D, RGB-D SLAM, and Scenes11 datasets.

Setting	Abs Rel	Sq Rel	RMSE	R_{log}	1.25	1.25^2	
w/o GRU	0.058	0.258	2.953	0.097	0.955	0.992	
w/o Alter	0.055	0.247	2.952	0.094	0.959	0.992	
w/o Cost	0.065	0.324	3.270	0.112	0.940	0.988	
Cost volume	0.049	0.214	2.804	0.086	0.966	0.994	
Full-setting	0.047	0.199	2.629	0.082	0.970	0.994	
Infer iterations	0	0.094	0.529	4.014	0.150	0.891	0.974
	4	0.059	0.266	2.992	0.099	0.951	0.992
	8	0.049	0.208	2.687	0.084	0.968	0.994
	16	0.046	0.198	2.623	0.081	0.970	0.994
	24	0.046	0.199	2.626	0.082	0.970	0.994

Table 4: Ablation study on the KITTI dataset. The first six metrics of those used in Table 1 are reported here.

4.4. Ablation Study

To inspect the effect of our framework, we evaluate each module of our model on the KITTI dataset and present the results in Table 4.

GRU module. The core module of our framework is the recurrent optimizer. To see how the recurrent module helps the optimization, we replace the GRU block with three convolutional layers. In the training, the depth error decreases to 0.058 in the first few epochs but then the network diverges. We think this is because the gate mechanism not only avoids the gradient explosion but also regularizes the optimization and makes the convergence stable. Furthermore, historical information is leveraged to guide the updating to avoid diverging directions.

Alternant update. It is important to alternatively update the depth and pose to decouple their influence in the feature-metric error. To see how they influence each other, we train a model where the optimizer predicts the depth and pose simultaneously. The depth accuracy in this setting is almost as poor as the one without GRU. This alternation is critical, for instance, when updating the depth, the training of the depth optimizer will be confused if the pose can be changed at the same time.

Cost Volume. One of the advantages of our method is that we do not need a heavy cost volume for optimization.

Here, we also replace the feature-metric error with a $H \times W \times 64$ cost volume as the minimization object. The cost volume is in a cascaded structure, i.e, in each stage the depth range of the volume is dynamically adjusted according to the last estimated depth. From the results shown in Table 4, the performance of using this heavy cost volume is similar to using the cost map, which proves that employing information in temporal domain can make up the lack of neighborhood information in spatial domain. Also, we test the performance of a model without the cost input. As expected, the error of the depth estimation is large since the optimizer loses the objective to minimize.

Iteration times. Until now, we only use 12 iterations of recurrent optimization for all experiments. We could also vary the number of iterations during inference. Here, we test different iteration numbers in the inference. Zero iteration means we do not update the initial depth and pose at all. According to the results in Table 4, our optimizer already outputs decent results after 4 iterations and predicts accurate results after 8 iterations, after which the depths are further refined with more iterations. This demonstrates that our optimizer has learned to optimize the estimation step by step. A model trained with a fixed number of iterations can be applied with more iterations in real applications to obtain finer results.

5. Conclusion

In this work, we have proposed a zeroth-order deep recurrent optimizer for addressing the structure from motion problem. Two gated recurrent units have been introduced to serve as an optimizer considering both the spatial neighbor information and the temporal historical trajectories, such that the heavy cost volume could be replaced by a lightweight cost, and the gradient is not needed to be explicitly calculated in this end-to-end optimizer. The experiments have demonstrated our approach outperforms all previous methods on both the outdoor and indoor datasets, in both the supervised and self-supervised settings, which suggests that leveraging the information in the time domain can make up the lack of information in the spatial domain for an optimization problem.

References

- [1] Jonas Adler and Ozan Öktem. Solving ill-posed inverse problems using iterative deep neural networks. *Inverse Problems*, 33(12):124007, 2017. 2
- [2] Akshay Agrawal, Brandon Amos, Shane Barratt, Stephen Boyd, Steven Diamond, and Zico Kolter. Differentiable convex optimization layers. In *Advances in Neural Information Processing Systems*, pages 9558–9570, 2019. 2
- [3] Brandon Amos and J Zico Kolter. Optnet: Differentiable optimization as a layer in neural networks. In *International Conference on Machine Learning*, pages 136–145. PMLR, 2017. 2
- [4] Jia-Wang Bian, Zhichao Li, Naiyan Wang, Huangying Zhan, Chunhua Shen, Ming-Ming Cheng, and Ian Reid. Unsupervised scale-consistent depth and ego-motion learning from monocular video. In *Thirty-third Conference on Neural Information Processing Systems (NeurIPS)*, 2019. 2
- [5] Jia-Wang Bian, Zhichao Li, Naiyan Wang, Huangying Zhan, Chunhua Shen, Ming-Ming Cheng, and Ian Reid. Unsupervised scale-consistent depth and ego-motion learning from monocular video. In *Thirty-third Conference on Neural Information Processing Systems (NeurIPS)*, 2019. 2
- [6] Michael Bloesch, Jan Czarnowski, Ronald Clark, Stefan Leutenegger, and Andrew J Davison. Codeslam—learning a compact, optimisable representation for dense visual slam. In *Proceedings of the IEEE conference on computer vision and pattern recognition*, pages 2560–2568, 2018. 1
- [7] Michael Bloesch, Tristan Laidlow, Ronald Clark, Stefan Leutenegger, and Andrew J Davison. Learning meshes for dense visual slam. In *Proceedings of the International Conference on Computer Vision*, pages 5855–5864, 2019. 1
- [8] Angel X Chang, Thomas Funkhouser, Leonidas Guibas, Pat Hanrahan, Qixing Huang, Zimo Li, Silvio Savarese, Manolis Savva, Shuran Song, Hao Su, et al. Shapenet: An information-rich 3d model repository. *arXiv preprint arXiv:1512.03012*, 2015. 7
- [9] Yutian Chen, Matthew W Hoffman, Sergio Gómez Colmenarejo, Misha Denil, Timothy P Lillicrap, Matt Botvinick, and Nando Freitas. Learning to learn without gradient descent by gradient descent. In *Proceedings of the International Conference on Machine Learning*, pages 748–756. PMLR, 2017. 2
- [10] Yuhua Chen, Cordelia Schmid, and Cristian Sminchisescu. Self-supervised learning with geometric constraints in monocular video: Connecting flow, depth, and camera. In *Proceedings of the International Conference on Computer Vision*, pages 7063–7072, 2019. 6
- [11] Junyoung Chung, Caglar Gulcehre, KyungHyun Cho, and Yoshua Bengio. Empirical evaluation of gated recurrent neural networks on sequence modeling. *arXiv preprint arXiv:1412.3555*, 2014. 2
- [12] Ronald Clark, Michael Bloesch, Jan Czarnowski, Stefan Leutenegger, and Andrew J Davison. Ls-net: Learning to solve nonlinear least squares for monocular stereo. *arXiv preprint arXiv:1809.02966*, 2018. 1, 2, 8
- [13] Angela Dai, Angel X. Chang, Manolis Savva, Maciej Halber, Thomas Funkhouser, and Matthias Nießner. Scannet: Richly-annotated 3d reconstructions of indoor scenes. In *Proceedings of the IEEE Conference on Computer Vision and Pattern Recognition*, 2017. 6
- [14] David Eigen, Christian Puhrsch, and Rob Fergus. Depth map prediction from a single image using a multi-scale deep network. In *Advances in Neural Information Processing Systems*, pages 2366–2374, 2014. 1, 2, 6
- [15] Jakob Engel, Thomas Schöps, and Daniel Cremers. Lsdslam: Large-scale direct monocular slam. In *Proceedings of the European Conference on Computer Vision*, pages 834–849. Springer, 2014. 7
- [16] Lijie Fan, Wenbing Huang, Chuang Gan, Stefano Ermon, Boqing Gong, and Junzhou Huang. End-to-end learning of motion representation for video understanding. In *Proceedings of the IEEE Conference on Computer Vision and Pattern Recognition*, pages 6016–6025, 2018. 2
- [17] Huan Fu, Mingming Gong, Chaohui Wang, Kayhan Batmanghelich, and Dacheng Tao. Deep ordinal regression network for monocular depth estimation. In *Proceedings of the IEEE Conference on Computer Vision and Pattern Recognition*, pages 2002–2011, 2018. 1, 2, 6
- [18] Clément Godard, Oisín Mac Aodha, Michael Firman, and Gabriel J Brostow. Digging into self-supervised monocular depth estimation. In *Proceedings of the International Conference on Computer Vision*, pages 3828–3838, 2019. 2, 6
- [19] Clément Godard, Oisín Mac Aodha, Michael Firman, and Gabriel J Brostow. Digging into self-supervised monocular depth estimation. In *Proceedings of the International Conference on Computer Vision*, pages 3828–3838, 2019. 5
- [20] Xiaodong Gu, Zhiwen Fan, Siyu Zhu, ZuoZhuo Dai, Feitong Tan, and Ping Tan. Cascade cost volume for high-resolution multi-view stereo and stereo matching. In *Proceedings of the IEEE Conference on Computer Vision and Pattern Recognition*, pages 2495–2504, 2020. 2
- [21] Vitor Guizilini, Rares Ambrus, Sudeep Pillai, Allan Raventos, and Adrien Gaidon. 3d packing for self-supervised monocular depth estimation. In *Proceedings of the IEEE Conference on Computer Vision and Pattern Recognition*, pages 2485–2494, 2020. 1, 2, 6
- [22] Kaiming He, Xiangyu Zhang, Shaoqing Ren, and Jian Sun. Deep residual learning for image recognition. In *Proceedings of the IEEE Conference on Computer Vision and Pattern Recognition*, pages 770–778, 2016. 3
- [23] Dinesh Jayaraman and Kristen Grauman. Learning image representations tied to ego-motion. In *Proceedings of the IEEE International Conference on Computer Vision*, pages 1413–1421, 2015. 1
- [24] Marvin Klingner, Jan-Aike Termöhlen, Jonas Mikolajczyk, and Tim Fingscheidt. Self-supervised monocular depth estimation: Solving the dynamic object problem by semantic guidance. In *Proceedings of the European Conference on Computer Vision*, pages 582–600. Springer, 2020. 2
- [25] Yevhen Kuznetsov, Jörg Stückler, and Bastian Leibe. Semi-supervised deep learning for monocular depth map prediction. In *Proceedings of the IEEE Conference on Computer Vision and Pattern Recognition*, pages 2215–2223, 2017. 6
- [26] Jin Han Lee, Myung-Kyu Han, Dong Wook Ko, and Il Hong Suh. From big to small: Multi-scale local planar

- guidance for monocular depth estimation. *arXiv preprint arXiv:1907.10326*, 2019. 1, 2
- [27] Ruihao Li, Sen Wang, Zhiqiang Long, and Dongbing Gu. Undeepvo: Monocular visual odometry through unsupervised deep learning. In *Proceedings of the IEEE International Conference on Robotics and Automation*, pages 7286–7291. IEEE, 2018. 2
- [28] Reza Mahjourian, Martin Wicke, and Anelia Angelova. Unsupervised learning of depth and ego-motion from monocular video using 3d geometric constraints. In *Proceedings of the IEEE Conference on Computer Vision and Pattern Recognition*, pages 5667–5675, 2018. 2
- [29] Anurag Ranjan, Varun Jampani, Lukas Balles, Kihwan Kim, Deqing Sun, Jonas Wulff, and Michael J Black. Competitive collaboration: Joint unsupervised learning of depth, camera motion, optical flow and motion segmentation. In *Proceedings of the IEEE Conference on Computer Vision and Pattern Recognition*, pages 12240–12249, 2019. 2, 6
- [30] Johannes L Schonberger and Jan-Michael Frahm. Structure-from-motion revisited. In *Proceedings of the IEEE Conference on Computer Vision and Pattern Recognition*, pages 4104–4113, 2016. 1
- [31] Jürgen Sturm, Nikolas Engelhard, Felix Endres, Wolfram Burgard, and Daniel Cremers. A benchmark for the evaluation of rgb-d slam systems. In *Proceedings of the IEEE/RSJ International Conference on Intelligent Robots and Systems*, pages 573–580. IEEE, 2012. 7
- [32] Chengzhou Tang and Ping Tan. Ba-net: Dense bundle adjustment networks. In *Proceedings of the International Conference on Learning Representations*, 2019. 1, 2, 3, 6, 7, 8
- [33] Zachary Teed and Jia Deng. Deepv2d: Video to depth with differentiable structure from motion. In *Proceedings of the International Conference on Learning Representations*, 2020. 1, 2, 6, 7
- [34] Zachary Teed and Jia Deng. Raft: Recurrent all-pairs field transforms for optical flow. In *Proceedings of the European Conference on Computer Vision*, pages 402–419. Springer, 2020. 1, 2, 3
- [35] Bill Triggs, Philip F McLauchlan, Richard I Hartley, and Andrew W Fitzgibbon. Bundle adjustment—a modern synthesis. In *International workshop on vision algorithms*, pages 298–372. Springer, 1999. 1
- [36] Benjamin Ummenhofer, Huizhong Zhou, Jonas Uhrig, Nikolaus Mayer, Eddy Ilg, Alexey Dosovitskiy, and Thomas Brox. Demon: Depth and motion network for learning monocular stereo. In *Proceedings of the IEEE Conference on Computer Vision and Pattern Recognition*, pages 5038–5047, 2017. 1, 2, 7, 8
- [37] Chaoyang Wang, José Miguel Buenaposada, Rui Zhu, and Simon Lucey. Learning depth from monocular videos using direct methods. In *Proceedings of the IEEE Conference on Computer Vision and Pattern Recognition*, pages 2022–2030, 2018. 2
- [38] Yang Wang, Peng Wang, Zhenheng Yang, Chenxu Luo, Yi Yang, and Wei Xu. Unos: Unified unsupervised optical-flow and stereo-depth estimation by watching videos. In *Proceedings of the IEEE Conference on Computer Vision and Pattern Recognition*, pages 8071–8081, 2019. 2
- [39] Zhou Wang, Alan C Bovik, Hamid R Sheikh, Eero P Simoncelli, et al. Image quality assessment: from error visibility to structural similarity. *IEEE Transactions on Image Processing*, 13(4):600–612, 2004. 5
- [40] Xingkui Wei, Yinda Zhang, Zhuwen Li, Yanwei Fu, and Xiangyang Xue. Deepsfm: Structure from motion via deep bundle adjustment. In *Proceedings of the European Conference on Computer Vision*, pages 230–247. Springer, 2020. 1, 2, 8
- [41] Jianxiong Xiao, Andrew Owens, and Antonio Torralba. Sun3d: A database of big spaces reconstructed using sfm and object labels. In *Proceedings of the International Conference on Computer Vision*, pages 1625–1632, 2013. 7
- [42] Nan Yang, Rui Wang, Jorg Stuckler, and Daniel Cremers. Deep virtual stereo odometry: Leveraging deep depth prediction for monocular direct sparse odometry. In *Proceedings of the European Conference on Computer Vision*. 2
- [43] Yao Yao, Zixin Luo, Shiwei Li, Tian Fang, and Long Quan. Mvsnet: Depth inference for unstructured multi-view stereo. In *Proceedings of the European Conference on Computer Vision*, pages 767–783, 2018. 2
- [44] Zhichao Yin and Jianping Shi. Geonet: Unsupervised learning of dense depth, optical flow and camera pose. In *Proceedings of the IEEE Conference on Computer Vision and Pattern Recognition*, pages 1983–1992, 2018. 2
- [45] Zehao Yu and Shenghua Gao. Fast-mvsnet: Sparse-to-dense multi-view stereo with learned propagation and gaussian refinement. In *Proceedings of the IEEE/CVF Conference on Computer Vision and Pattern Recognition*, pages 1949–1958, 2020. 1
- [46] Huangying Zhan, Ravi Garg, Chamara Saroj Weerasekera, Kejie Li, Harsh Agarwal, and Ian Reid. Unsupervised learning of monocular depth estimation and visual odometry with deep feature reconstruction. In *Proceedings of the IEEE Conference on Computer Vision and Pattern Recognition*, pages 340–349, 2018. 2
- [47] Wang Zhao, Shaohui Liu, Yezhi Shu, and Yong-Jin Liu. Towards better generalization: Joint depth-pose learning without posenet. In *Proceedings of the IEEE Conference on Computer Vision and Pattern Recognition*, pages 9151–9161, 2020. 2
- [48] Huizhong Zhou, Benjamin Ummenhofer, and Thomas Brox. Deeptam: Deep tracking and mapping. In *Proceedings of the European Conference on Computer Vision*, pages 822–838, 2018. 1, 2
- [49] Tinghui Zhou, Matthew Brown, Noah Snavely, and David G Lowe. Unsupervised learning of depth and ego-motion from video. In *Proceedings of the IEEE Conference on Computer Vision and Pattern Recognition*, pages 1851–1858, 2017. 2, 6
- [50] Yuliang Zou, Zelun Luo, and Jia-Bin Huang. Df-net: Unsupervised joint learning of depth and flow using cross-task consistency. In *Proceedings of the European Conference on Computer Vision*, pages 36–53, 2018. 2

DRO: Deep Recurrent Optimizer for Structure-from-Motion

Appendix

A. Network Structure

To illustrate the details of our framework, we display our network structure in Figure 1. The first module is the initialization block. Two base feature networks sharing the same parameters are employed to extract the features \mathcal{F}_0 and \mathcal{F}_i of input images, which are leveraged to estimate the initial depth and pose. The feature networks are using ResNet18 [2] as the backbone, and the output heads are composed of two convolutional layers. For the pose head, a global average pooling layer is also adopted. Then, based on the current estimated depth, pose, and features \mathcal{F}_0 and \mathcal{F}_i , a cost C_i is constructed. Afterward, the contextual networks use the same structure as the base feature networks to extract the contextual features \mathcal{F}_0^c and \mathcal{F}_i^c , which are fed into the GRU modules. The GRU optimizers take the contextual features, the cost, and the current estimated depth or pose in, to estimate the variables increments.

B. Time and Memory Consumption

One of the advantages of our approach compared to cost-volume-based methods is the efficiency in computation and memory consumption. To see how lightweight our optimizer is, we compare it in different numbers of iterations with DeepV2D [4], which is the method performing best before ours. We test the GPU memory occupancy and the network forward time of different numbers of iterations in the inference, as presented in Table 1. All experiments are conducted on the KITTI dataset with an Nvidia GTX 2080 Ti GPU.

We try two strategies for the model running different numbers of iterations. The first one is directly applying the model trained with 12 iterations and only adjusting the number of iterations in the inference. The second one is learning a new model from scratch with fewer iterations in the training, which is denoted with “*” in Table 1. The results show that the retrained models perform slightly better. Compared to DeepV2D, both strategies achieve better performance in four iterations, with much less GPU Memory and inference time. The model retrained from scratch with two iterations can even outperform DeepV2D. This allows our model to be applied to small-memory mobile devices and be employed

Models		Resolution	Memory	Time	Abs Rel
DeepV2D [4]		192×1088	6.75 G	1.49 s	0.064
DRO	iterate 12	320×960	1.16 G	0.12 s	0.047
	iterate 8	320×960	1.15 G	0.086 s	0.049
	iterate 4	320×960	1.15 G	0.049 s	0.059
	iterate 0	320×960	1.11 G	0.011 s	0.094
DRO (retrained)	iterate 4*	320×960	1.15 G	0.049 s	0.054
	iterate 3*	320×960	1.13 G	0.042 s	0.056
	iterate 2*	320×960	1.12 G	0.032 s	0.060
	iterate 1*	320×960	1.12 G	0.022 s	0.066
	iterate 0*	320×960	1.11 G	0.011 s	0.081

Table 1: Efficiency experiments on the KITTI dataset. Resolution of the input images, GPU Memory consumption, network forward time, and the relative absolute error of the depth map are reported. “*” denotes retrained from scratch.

in real-time applications.

C. More Views

In an SfM task, the depths and poses could be estimated with arbitrary number of images. In previous experiments, however, only two images are used for inference for a fair comparison with other methods. Inference with more frames should predict better depths and poses, since there is more information provided. Hence, we feed five images into our model in the inference without retraining to see if it can perform better, as presented in Table 2. Compared to the results of using two views, the performance of using five views is better as expected.

D. More Visualization Results

We display more qualitative results on the SUN3D dataset, RGB-D SLAM dataset, and Scenes11 dataset. The depth maps obtained with our supervised model and DeepSfM [5] are presented in Figure 2 and Figure 3, from which we can see that our model predicts smoother and cleaner depth maps.

In addition, our model can be trained in either the supervised setting or the self-supervised setting. The depth

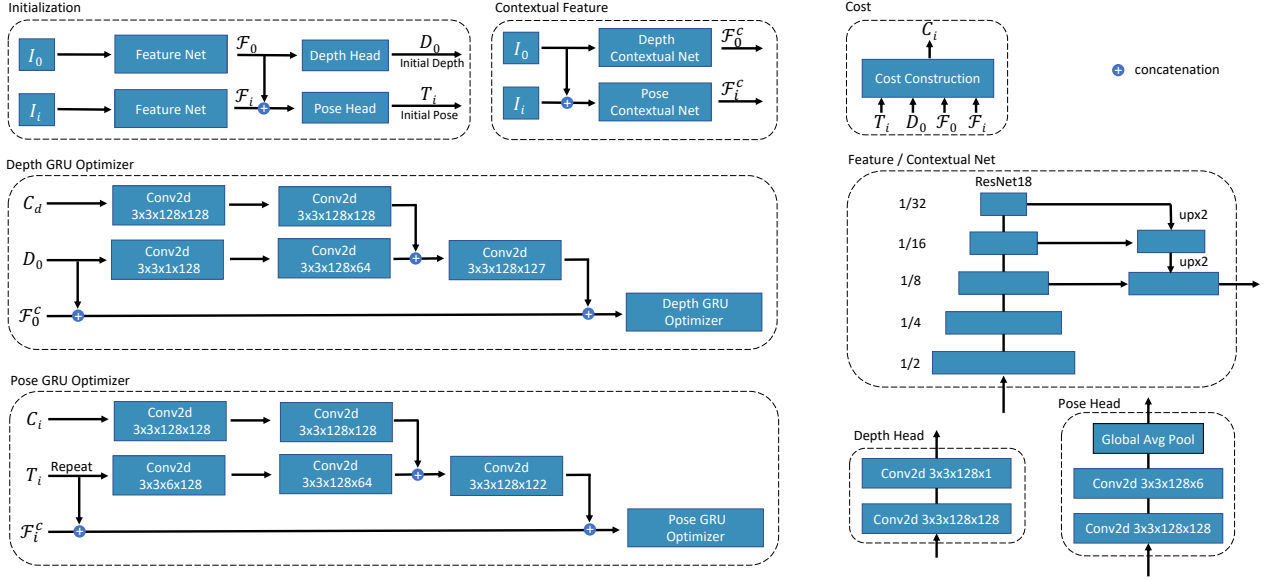


Figure 1: The details of modules in our framework. The reference image I_0 and neighbor image I_i are fed into the base feature networks to extract the features \mathcal{F}_0 and \mathcal{F}_i , which are then input to the depth head and pose head to predict the initial depth and initial pose. Afterward, the contextual networks extract the contextual features \mathcal{F}_0^c and \mathcal{F}_i^c , which are fed into the GRU optimizers together with the depth, pose, and cost. The details of the cost construction, feature networks, and output heads are also presented.

Method	#View	Abs Rel	Sq Rel	RMSE	RMSE _{log}	SI Inv	Rot (deg)	Tr (deg)	Tr (cm)
BANet [3]	2	0.161	0.092	0.346	0.214	0.184	1.018	20.577	3.390
BANet [3]	5	0.091	0.058	0.223	0.147	0.137	1.009	14.626	2.365
DeepV2D [4]	2	0.069	0.018	0.196	0.099	0.097	0.692	11.731	1.536
DeepV2D [4]	5	0.057	0.010	0.168	0.080	0.077	0.628	10.800	1.373
DRO (ours)	2	0.053	0.017	0.168	0.081	0.079	0.473	9.219	1.160
DRO (ours)	5	0.049	0.015	0.157	0.075	0.074	0.463	8.871	1.139

Table 2: Quantitative results of using five views on the ScanNet dataset. Five metrics of the depth and three metrics of the pose are reported.

maps and poses estimated by our self-supervised model are already more accurate than that of many supervised models. To inspect how our self-supervised model performs, we compare the results of it with our supervised model and self-supervised PackNet-SfM [1] in Figure 4. Compared to PackNet-SfM, our model predicts better details of small-size and distinct objects, and estimates correct depth of the hard objects like the white guideboard. Compared to the supervised model, there is still a gap but the gap is not large. Sometimes the self-supervised model can estimate better depth than the supervised model.

References

- [1] Vitor Guizilini, Rares Ambrus, Sudeep Pillai, Allan Raventos, and Adrien Gaidon. 3d packing for self-supervised monocular depth estimation. In *Proceedings of the IEEE Conference on Computer Vision and Pattern Recognition*, pages 2485–2494, 2020. 2
- [2] Kaiming He, Xiangyu Zhang, Shaoqing Ren, and Jian Sun. Deep residual learning for image recognition. In *Proceedings of the IEEE Conference on Computer Vision and Pattern Recognition*, pages 770–778, 2016. 1
- [3] Chengzhou Tang and Ping Tan. Ba-net: Dense bundle adjustment networks. In *Proceedings of the International Conference on Learning Representations*, 2019. 2
- [4] Zachary Teed and Jia Deng. Deepv2d: Video to depth with differentiable structure from motion. In *Proceedings of the International Conference on Learning Representations*, 2020. 1, 2
- [5] Xingkui Wei, Yinda Zhang, Zhuwen Li, Yanwei Fu, and Xiangyang Xue. Deepsfm: Structure from motion via deep bundle adjustment. In *Proceedings of the European Conference on Computer Vision*, pages 230–247. Springer, 2020. 1

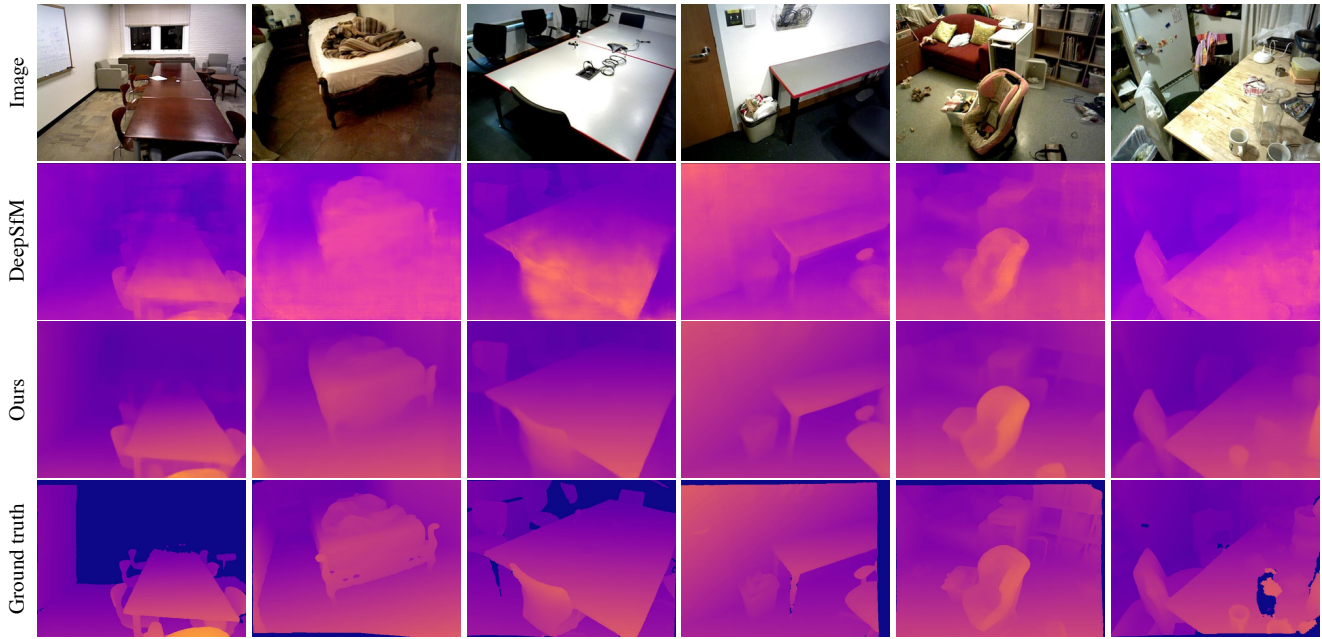


Figure 2: Qualitative results of on the SUN3D dataset. The depth maps obtained by DeepSfM and our approach are displayed with the input images and ground-truth depth maps.

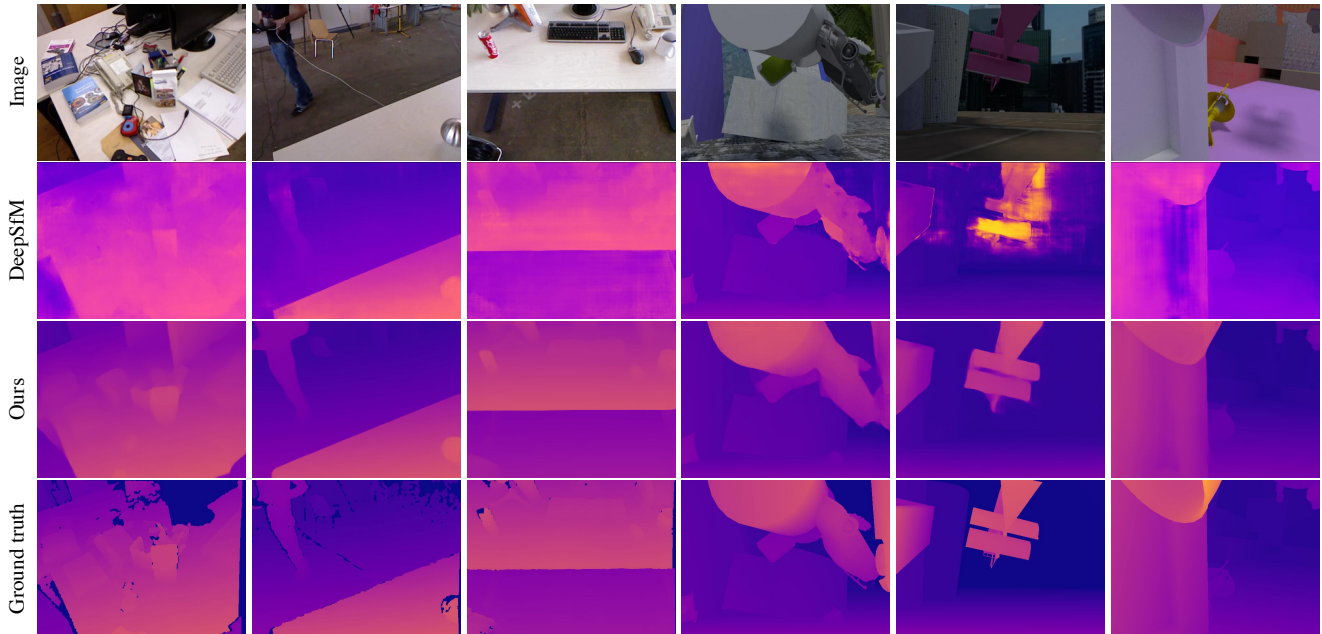


Figure 3: Qualitative results on the RGB-D and Scenes11 dataset. The left three columns are results of RGB-D images and the right three are those of Scenes11 images. The depth maps obtained by DeepSfM and our approach are displayed with the input images and ground-truth depth maps.

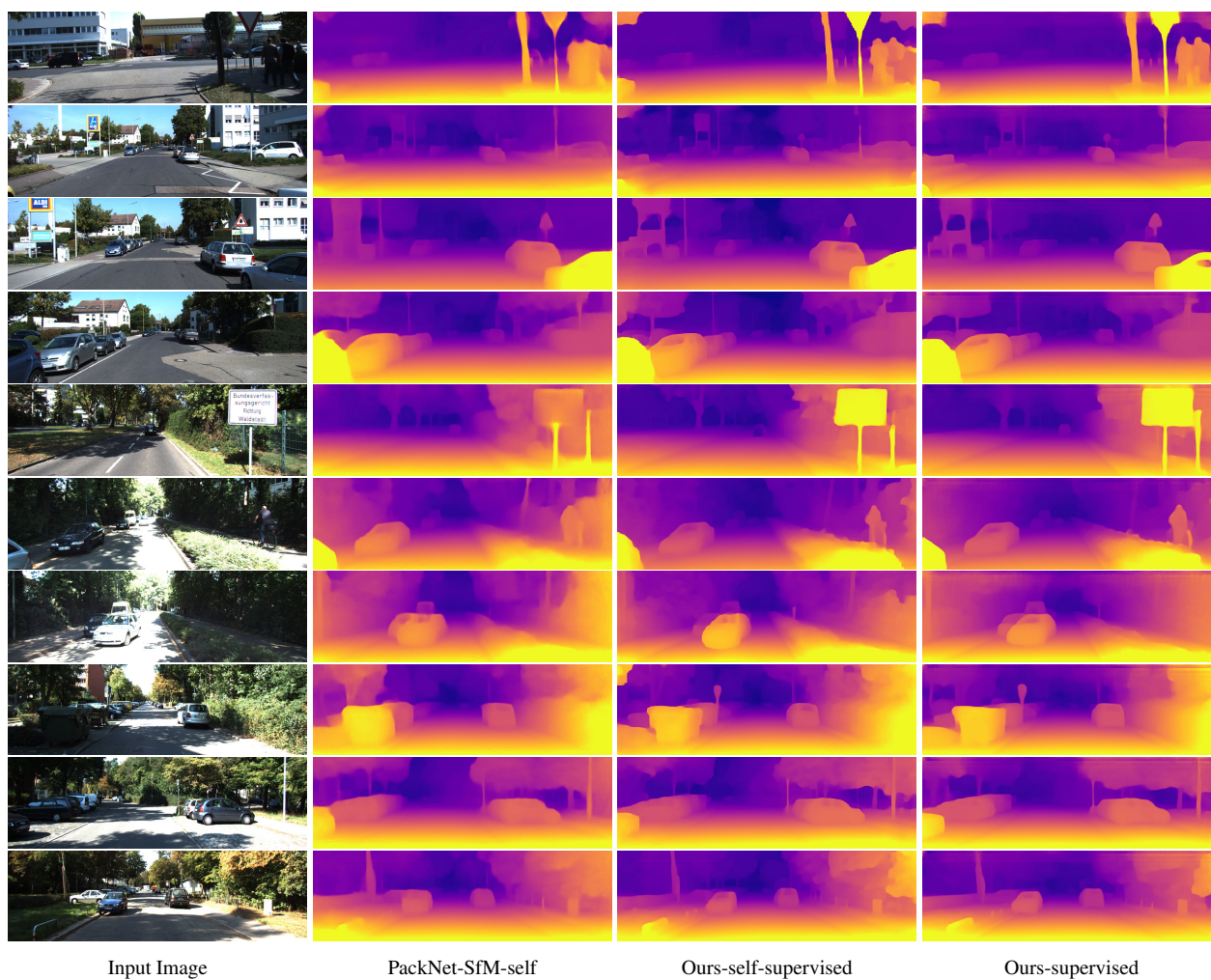


Figure 4: Qualitative results of self-supervised models and our supervised model on the KITTI dataset. “PackNet-SfM-self” is the model of PackNet-SfM trained in their self-supervised setting.